An Energy and Emissions Conscious Adaptive Cruise Controller for a Connected Automated Diesel Truck

Chunan Huang, Rasoul Salehi, Tulga Ersal and Anna. G. Stefanopoulou

Department of Mechanical Engineering, 1231 Beal Ave., University of Michigan, Ann Arbor, MI, 48109 USA

ARTICLE HISTORY
Compiled November 9, 2019

ABSTRACT

Conventional speed planning for connected automated vehicles (CAVs) adopts an energy-centric perspective and improves fuel economy by means of reducing the power loss due to braking and operating the engine at its high efficiency region. This paper considers a simulated connected automated truck with a diesel powertrain and a selective catalytic reduction (SCR) system for the treatment of NOx emissions, and first shows that a 20% fuel economy improvement is followed by up to 50% increase in NOx emissions with conventional speed planning due to its sole focus on energy that neglects emissions. Then, a novel model predictive controller (MPC) is designed for concurrent treatment of energy and emissions within speed planning of the CAV. Details of this energy and emissions conscious (E^2C) MPC design is described including the vehicle, powertrain and emissions model development, selection of the appropriate objective function and its parameters for acceptable optimality, and computational performance. Simulation results of the E^2C-MPC over multiple drive cycles are presented to demonstrate the robust performance of the controller. The results show 5-15% improvement in the fuel economy with a corresponding 0-25% reduction in NOx emissions for different drive cycles without requiring re-calibration for each test cycle.

KEYWORDS
Connected automated vehicles; model predictive control; diesel powertrain; fuel efficiency; NOx emissions control; robustness to drive cycle

1. Introduction

Automated driving assistance systems such as adaptive cruise control provide opportunities to reduce fuel consumption and emissions by adjusting the speed of a connected automated vehicle in a given traffic condition predicted using vehicle-to-vehicle (V2V) or vehicle-to-infrastructure (V2I) communication [1–7]. With an energy-centric perspective, conventional speed planning methods for CAVs focus on improving fuel economy. Extensive research exists on CAV speed planning for better fuel economy, with a summary and quantification of different methods presented in [1]. For example, platooning is a strategy for CAVs to reduce fuel consumption through reduced air drag due to the low-distance car following policy in a platoon [1,8]. Another extensively explored method is look-ahead speed planning to achieve eco-driving with reduced acceleration and deceleration when the CAV is following a lead vehicle [3–6,9–12]. In this case, a flexible following distance policy is adopted to turn the

CONTACT Tulga Ersal. Email: tersal@umich.edu

CAV speed into a design variable that is then optimized to maximize fuel economy by reducing accelerating/braking events while taking into account the leader's maneuvers in given traffic and road conditions [3,6]. Including the nonlinear engine fuel efficiency map in the CAV speed planning leads to additional fuel savings when used with an available drive cycle preview [4,5,12,13].

Along with fuel consumption, emission reduction is another crucial performance metric for a vehicle, which is highly demanded by federal organizations [14]. Tailpipe emission of a vehicle strongly depends on the aftertreatment system (ATS) conditions and its capability to eliminate the harmful species from the exhaust gas. Moreover, the catalytic ATS activity depends on its surface temperature, such that reducing the engine load can result in low SCR temperature and ultimately cut off the urea solution injection with a consequent increase in tailpipe NOx emissions [15] even though it is a fuel-efficient strategy [5,13]. In [3,16], the authors suggest integrating the reduction of engine-out NOx emission with the fuel consumption minimization problem to find a variable distance car following policy, or an optimal velocity trajectory with the information of future road grade. Authors of [17] considered the emissions reduction problem for a chain of automated vehicles in a congested platoon, and showed that reduced emissions and travel delay could be achieved through longitudinal control. However, in these previous works the aftertreatment temperature control is ignored, which is necessary to control the tailpipe emissions of diesel trucks [5]. As the literature on control of hybrid electric vehicles demonstrates, fuel consumption and emissions can be successfully balanced if the effect of aftertreatment on reducing tailpipe emissions is taken into account explicitly [18–20]. However, a similar comprehensive framework does not yet exist for speed planning in CAVs. Note that the framework described in this paper is not aiming at the federal tests, as current federal regulations only allow very limited speed deviations when doing fuel economy and emission assessment, whereas the described speed planning framework will lead to larger speed deviations.

Recognizing the gap identified above, this paper builds on the prior work presented in [5,13] that demonstrates the importance of tailpipe NOx emission control and extends it to introduce a novel energy and emissions conscious predictive speed planning framework to optimally balance the goals of reducing fuel consumption and emissions in connected automated diesel trucks with improved possibility for real-time implementation. Within the scope of this paper, it is assumed that the predictive information within each prediction horizon is known accurately, and that no other traffic limitation exists except for the the constraints considered in the control framework. Thus, the original contribution of this paper is an energy and emissions conscious model predictive control formulation that is referred to as E^2C-MPC.

To this end, a formulation that can work with models of reduced order and complexity is presented. A detailed analysis of the powertrain and the aftertreatment is given to explain the intuition behind the new E^2C-MPC controller. In addition, the controller with a fixed calibration is tested over different drive cycles, showing promising performance for fuel savings without increasing vehicle emissions for all test cycles considered.

The rest of the paper is organized as follows. In Section 2, the vehicle and its aftertreatment models are developed and validated with experiments. The MPC framework is presented in Section 3. Section 4 demonstrates the tradeoff between tailpipe NOx and fuel consumption reduction with a conventional speed planning approach in which the emissions control is ignored. This conventional approach is referred to as energy conscious MPC (EC-MPC) due to its sole focus on fuel economy. In Section 5, the development of the new predictive controller is presented, with analysis on controller performance, computational effort and robustness to different drive cycles, as mentioned above. This section is the novel contribution of this paper compared to [5,13]. In Section 6, the outstanding challenges are discussed. Finally, the paper is concluded in Section 7.

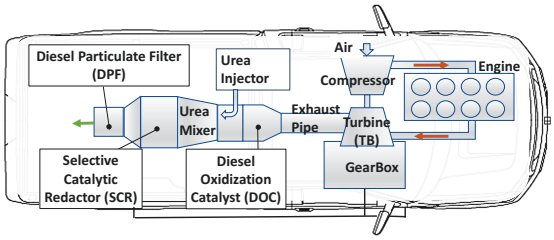

(a) Engine and aftertreatment system configuration schematically shown on the vehicle.

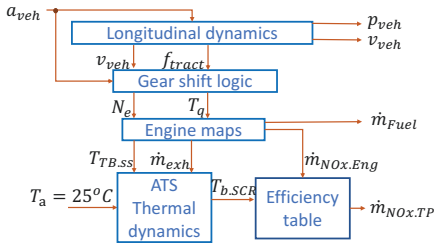

(b) Structure of the developed vehicle model.

Figure 1. Vehicle schematic and its model structure for the diesel powered vehicle considered in this paper.

2. Vehicle model

A vehicle model including longitudinal dynamics, powertrain steady-state maps and the thermal dynamics of the aftertreatment system is developed and presented in this section. This model is used for the development of model-based controllers in Sections 4 and 5, as well as simulating fuel consumption and tailpipe emissions of the vehicle.

The vehicle studied in this work, the medium-duty Ford F-250 truck, and its model structure is shown in Figure 1. The aftertreatment system includes a Diesel Oxidation Catalyst (DOC), a Selective Catalytic Reduction (SCR) block, and a Diesel Particulate Filter (DPF) as shown in Figure 1(a). The vehicle model in Figure 1(b) includes a single varying input, namely, the vehicle acceleration a_{veh}, and the key outputs are the vehicle position p_{veh}, speed v_{veh}, fuel consumption rate $\dot{m}_{\text{fuel}}$ and tailpipe NOx emissions rate $\dot{m}_{\text{NOx.TP}}$. The details of each submodel in Figure 1(b) are described next.

2.1. Longitudinal dynamics

Assuming the vehicle as a point mass system, the vehicle state vector $\left[p_{\text{veh}}, v_{\text{veh}}\right]^T$, which comprises vehicle position and speed, is calculated using:

$$\begin{bmatrix} \dot{p}_{\text{veh}} \\ \dot{v}_{\text{veh}} \end{bmatrix} = \begin{bmatrix} 0 & 1 \\ 0 & 0 \end{bmatrix} \begin{bmatrix} p_{\text{veh}} \\ v_{\text{veh}} \end{bmatrix} + \begin{bmatrix} 0 \\ 1 \end{bmatrix} a_{\text{veh}}, \tag{1}$$

given the vehicle acceleration a_{veh} as the input.

With the vehicle speed v_{veh} and acceleration a_{veh}, the demanded vehicle traction force f_{tract} is calculated using the longitudinal dynamics model:

$$f_{\text{tract}} = M_{\text{v}} a_{\text{veh}} + f_{\text{rr}} + f_{\text{air}}. \tag{2}$$

In (2), M_{v} represents the vehicle mass, and f_{rr} and f_{air} represent the rolling resistance and the air drag resistance, respectively. They are calculated as:

$$f_{\text{rr}} = C_{\text{R}} M_{\text{v}} g \, \mathbf{sgn}(v_{\text{veh}}), \tag{3}$$

$$f_{\text{air}} = 0.5 \rho_{\text{air}} A_{\text{f}} C_{\text{d}} v_{\text{veh}} |v_{\text{veh}}|, \tag{4}$$

with C_{R} being the rolling resistance coefficient, ρ_{air} and C_{d} the air density and air drag co-

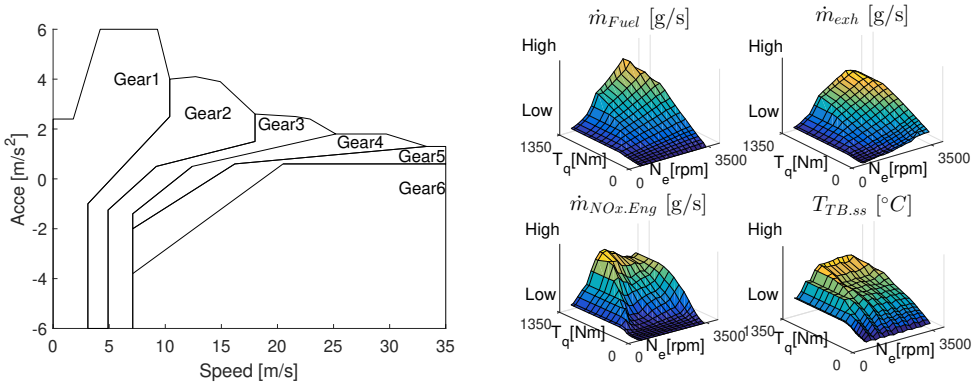

(a) Gear level map.

(b) Look-up tables used to calculate engine outputs.

Figure 2. Gear shift and engine maps used in the vehicle model.

efficient, and A_f the vehicle frontal area. In this work, the effect of road grade is ignored for simplicity.

2.2. Gear shift model

A unique gear level (GL) is assigned based on the vehicle speed v_veh and acceleration a_veh as shown in Figure 2(a). Then, the engine speed N_e and the calculated torque T_q are calculated as:

$$N_\mathrm{e} = F_\mathrm{R} G_\mathrm{R}(GL) \frac{1}{R_\mathrm{w}} v_\mathrm{veh}, \tag{5}$$

$$T_\mathrm{q} = \begin{cases} g_\mathrm{Tq}(f_\mathrm{tract} \frac{v_\mathrm{veh}}{N_e \eta_t}), & \text{if not at idle} \\ T_\mathrm{idle}, & \text{if at idle} \end{cases} \tag{6}$$

where F_R, $G_\mathrm{R}(GL)$ and R_w represent the final drive ratio, gear ratio at present gear level (GL) and wheel radius, respectively, and η_t represents the lumped transmission efficiency. g_Tq is a mapping from the physical engine torque to the non-negative calculated torque T_q that the manufacturer uses as input to the look-up tables. When the vehicle is stopped, the engine idle speed is set to be 600 rpm and the engine idle torque demand is a constant number T_idle.

2.3. Engine and efficiency models

Fuel rate $\dot{m}_\mathrm{fuel}$, exhaust flow rate $\dot{m}_\mathrm{exh}$, engine out NOx emission rate $\dot{m}_\mathrm{NOx.Eng}$ and steady state turbine out temperature $T_\mathrm{TB.ss}$ are calculated using look-up tables mapped with engine speed N_e and torque T_q, as shown in Figure 2(b). These maps are created validated and provided by the manufacturer. This calculation is based on the following three simplifying assumptions: (1) The engine air path dynamics are ignored, (2) the engine raw NOx contains only NO, and NO oxidization in diesel catalytic converter is ignored since DOC temperature is nearly always lower than 250 °C in the stabilized phase [21], (3) the SCR efficiency η_SCR is determined by an efficiency table for the NO conversion, based on SCR brick temperature $T_\mathrm{b.SCR}$ [21]. Based on these assumptions, tailpipe NOx emissions rate $\dot{m}_\mathrm{NOx.TP}$ is calculated as

$$\dot{m}_\mathrm{NOx.TP} = (1 - \eta_\mathrm{SCR}(T_\mathrm{b.SCR}))\dot{m}_\mathrm{NOx.Eng}, \tag{7}$$

where the calculation of SCR temperature $T_{\text{b.SCR}}$ is presented in the next section.

2.4. Aftertreatment system thermal dynamics model

To calculate the SCR brick temperature $T_{\text{b.SCR}}$ in (7), a complete thermal model, including that of turbine, DOC and SCR, is needed. A first-order lag is assumed for the dynamics of the turbine outlet gas temperature T_{TB}:

$$T_{\text{TB}} = \frac{1}{1+\tau s} T_{\text{TB.ss}}, \tag{8}$$

where τ is assumed to be inversely proportional to exhaust mass flow rate [22], i.e., $\tau \propto \frac{1}{\dot{m}_{\text{exh}}}$.

The DOC and SCR catalysts are modeled as thermal masses, and their thermal models are derived under the following assumptions: (1) Heat conduction from the exhaust gas into the catalytic brick is negligible compared with heat convection between them. (2) Axial heat diffusion in the fluid phase and axial conduction in the solid phase are ignored. (3) Heat capacity of the gas trapped in the catalytic brick is too small compared with that of the brick. Hence, there is no dynamics for the gas temperature inside the catalyst. (4) Heat radiations between the gas and the brick, and between the brick and the ambient are ignored based on the experimental validation results in the literature [23]. With these assumptions, the following first-order system is utilized to model the thermal dynamics of the DOC [23,24].

$$T_{\text{g.DOC}} = \frac{\frac{\dot{m}_{\text{exh}} C_{\text{pg}}}{V_{\text{DOC}}} T_{\text{in}_{\text{delay}}.\text{DOC}} + (h_1\alpha_1)_{\text{DOC}} T_{\text{b.DOC}}}{(h_1\alpha_1)_{\text{DOC}} + \frac{\dot{m}_{\text{exh}} C_{pg}}{V_{\text{DOC}}}}, \tag{9}$$

$$(1-\varepsilon_{\text{DOC}})\rho_{\text{b}} C_{\text{b}} \frac{dT_{\text{b.DOC}}}{dt} = (h_1\alpha_1)_{\text{DOC}}(T_{\text{g.DOC}} - T_{\text{b.DOC}}) - (h_2\alpha_2)_{\text{DOC}}(T_{\text{b.DOC}} - T_{\text{a}}), \tag{10}$$

where $T_{\text{g.DOC}}$ and $T_{\text{b.DOC}}$ are the DOC outlet gas and brick temperatures, ρ_{b} and C_{b} are the density and specific heat capacity of the monolith, ε_{DOC} is a parameter showing the fraction of the DOC open cross sectional area [25], C_{pg} is the specific heat capacity of the exhaust gas, V_{DOC} is the volume of the catalytic brick, h_1 and h_2 are the heat convection coefficients from the gas flow to the monolith, and from the block surface to the ambient, α_1 and α_2 are the corresponding geometric surface area-to-volume ratios [25], and T_{a} is the ambient temperature, which is set to be 25°C in this paper. Both h_1 and h_2 are assumed to be changing linearly depending on the exhaust mass flow rate.

$T_{\text{in}_{\text{delay}}.\text{DOC}}$ in (9) is calculated as:

$$T_{\text{in}_{\text{delay}}.\text{DOC}}(t) = T_{\text{TB}}(t - \Delta\tau_{\text{d.DOC}}), \tag{11}$$

and the variable $\Delta\tau_{\text{d.DOC}}$, which causes a dead-time in DOC temperature when engine operation condition changes, is defined by the following equation and calculated using an iterative method:

$$\int_{t-\Delta\tau_{\text{d.DOC}}}^{t} \frac{C_{pg}}{A_{\text{DOC}}(1-\varepsilon_{\text{DOC}})\rho_b C_b} \dot{m}_{\text{exh}} ds = c_{\text{d.DOC}}, \tag{12}$$

with $A_{\text{DOC}}(1-\varepsilon_{\text{DOC}})$ being the cross sectional wall area of DOC brick [24]. This equation corresponds to a transport phenomenon, with the integrand being the speed of flow, and the constant parameter $c_{\text{d.DOC}}$ is the distance that heat propagates in the DOC brick. The delay time $\Delta\tau_{\text{d.DOC}}$ accounts for a residence time needed for heat to propagate into the monolith.

It corresponds to a transport phenomenon according to a Plug-Flow assumption; see [24] for details. As shown in (9) and (10), the presented thermal model ignores exothermic reactions of CO and unburned hydrocarbons with oxygen in the DOC, which happens mainly when there is in-cylinder post injection.

The same model structure is considered to calculate the SCR output gas temperature $T_{\text{g.SCR}}$ and brick temperature $T_{\text{b.SCR}}$ because of the similar physical structures of SCR and DOC.

$$T_{\text{g.SCR}} = \frac{\frac{\dot{m}_{\text{exh}} C_{pg}}{V_{\text{SCR}}} T_{\text{in}_{\text{delay}}.\text{SCR}} + (h_1\alpha_1)_{\text{SCR}} T_{\text{b.SCR}}}{(h_1\alpha_1)_{\text{SCR}} + \frac{\dot{m}_{\text{exh}} C_{pg}}{V_{\text{SCR}}}}, \tag{13}$$

$$(1-\varepsilon_{\text{SCR}})\rho_{\text{b}} C_{\text{b}} \frac{dT_{\text{b.SCR}}}{dt} = (h_1\alpha_1)_{\text{SCR}}(T_{\text{g.SCR}} - T_{\text{b.SCR}}) - (h_2\alpha_2)_{\text{SCR}}(T_{\text{b.SCR}} - T_a), \tag{14}$$

$$T_{\text{in}_{\text{delay}}.\text{SCR}}(t) = T_{\text{g.DOC}}(t - \Delta\tau_{\text{d.SCR}}). \tag{15}$$

$\Delta\tau_{d.SCR}$ is calculated using a similar equation as (12) with different parameters identified for SCR. Furthermore, based on simulation results, the change of $\dot{m}_{\text{exh}}$ and $T_{\text{in}_{\text{delay}}.\text{SCR}}$ caused by urea solution injection are found to be small and are therefore ignored in the SCR model.

2.5. Model validation

The parameters in the above models are identified using measured vehicle speed, engine speed and torque, and aftertreatment gas temperatures for a MY2013 Ford F-250 Super-duty truck with a 6.7 L diesel engine when it is running a federal test procedure (FTP). Validation results for engine speed and torque prediction are shown in Figure 3. Due to the fact that this model does not include a torque converter, the simulated engine speed and torque during transient conditions are more oscillatory than the measured variables as shown in the second and third subplots in Figure 3. During slow transients and steady operation conditions, the model follows engine speed and torque trajectory sufficiently closely for the purposes of this study.

Figure 4 shows the validation results of the aftertreatment system gas temperatures compared with real vehicle measurements. Due to the delayed structure of the thermal dynamics presented in (9)-(15), temperature histories from the cold start phase are required as initial conditions in the DOC and SCR models in the stabilized phase. Thus, in all temperature calculations in this paper, simulations start from the starting point of the cold start phase to provide reasonable initial conditions for the stabilized phase of FTP. However, only the stabilized phase is used for comparison and verification, or for control purposes in Section 5. As observed, the gas temperature dynamics is effectively slowed down from T_{TB} to $T_{g.SCR}$. The thermal model sometimes misses the dynamics in Bag 1 as it does not include post-injection or water condensation effect. The root-mean-square errors for the turbine, the DOC and the SCR temperatures in Bag 2 are 9.0°C, 10.6°C, and 10.4°C, respectively. SCR efficiency traces calculated using the model and the measured SCR temperature are shown in Figure 5. Here we model the SCR efficiency using an efficiency table based on SCR temperature [26]. The root-mean-square error for efficiency is 1.12%. Thus, the model is considered to be accurate enough for the purpose of this paper.

3. General architecture for optimal vehicle speed planning

The speed trajectory of the CAV is optimized by a model predictive controller (MPC) when the vehicle is following a leader vehicle in urban or highway traffic. In this section, the overall

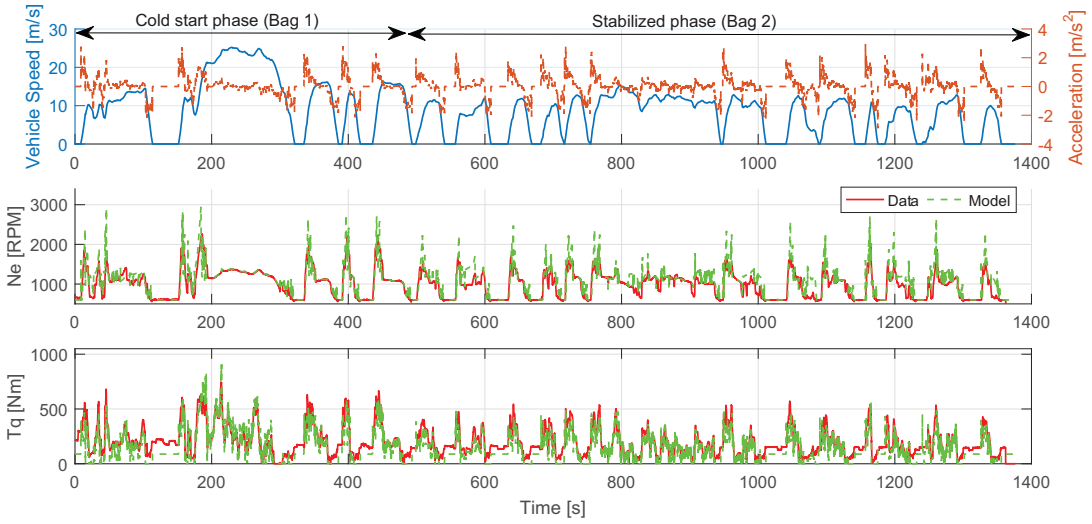

Figure 3. Validation results for the vehicle longitudinal model

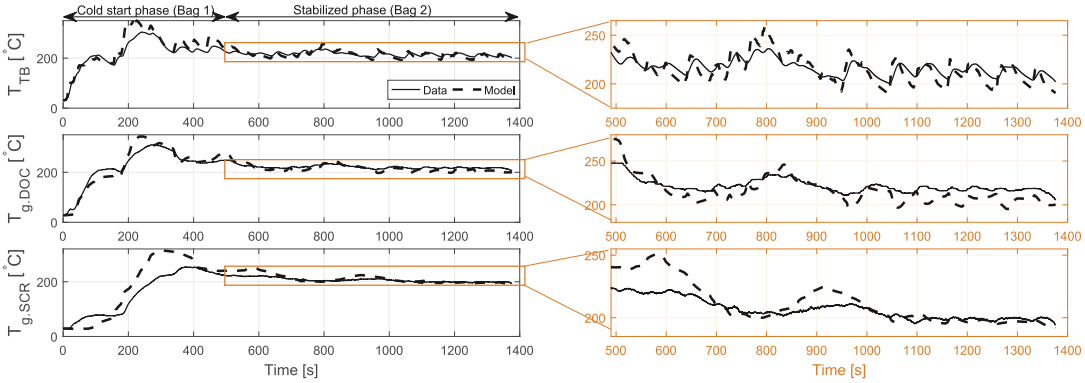

Figure 4. Thermal model validated over the standard FTP drive cycle.

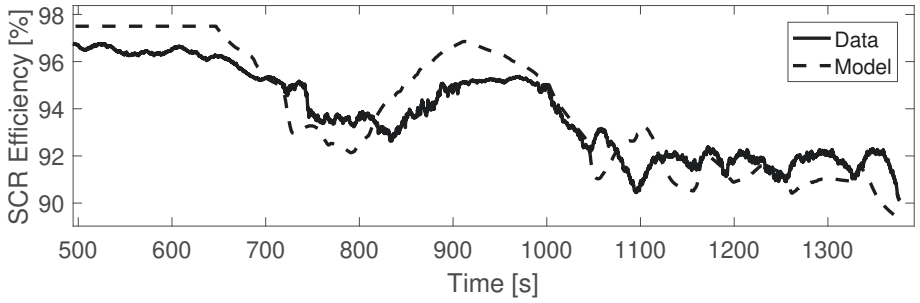

Figure 5. Comparison of SCR efficiency traces calculated with modeled SCR temperature and data over the standard FTP drive cycle.

structure of the designed MPC is described, and later in Sections 4 and 5, the optimizer is tailored respectively for the specific cases of the conventional energy-conscious speed planner EC-MPC as a baseline and the energy and emissions conscious planner E^{2}C-MPC as the new approach.

The predictive controller solves the following optimal control problem (OCP) to acquire the optimal input at each time step t:

$$\min_{U} \quad \mathbf{J}(t) = \sum_{k=0}^{N_\mathrm{P}-1} J(k|t) \tag{16}$$

where N_P is the number of samples in the prediction horizon, $\mathbf{J}$ is the optimization objective function, with several possible selections presented in later sections, and the optimization variable $U = \begin{bmatrix} a_\mathrm{veh}(0|t) & a_\mathrm{veh}(1|t) & \cdots & a_\mathrm{veh}((N_\mathrm{P}-1)|t) \end{bmatrix}^T$, is the evenly sampled vehicle acceleration over the prediction horizon, with a constant sampling time dt. Thus the prediction horizon is equal to $N_\mathrm{P} \cdot dt$. The notation $z(k|t)$ (here z is used to represent a generic variable) refers to the predicted value of the variable z at the k^{th} step in the prediction horizon, which is the predicted value at time $(t + k \cdot dt)$ given the information at time t.

The OCP is solved under the following constraints $\forall k = 0, 1, \ldots N_\mathrm{p} - 1$:

$$\begin{aligned} \underline{p}(v_\mathrm{l}(k \cdot dt + t + 1)) \leq & p_\mathrm{veh}(k+1|t) \leq \overline{p}(v_\mathrm{l}(k \cdot dt + t + 1)) \\ \underline{v_\mathrm{f}} \leq & v_\mathrm{veh}(k+1|t) \leq \overline{v_\mathrm{f}} \\ \underline{a_\mathrm{veh}} \leq & a_\mathrm{veh}(k|t) \leq \overline{a_\mathrm{veh}} \\ x(k+1|t) = & x(k|t) + dt \cdot f(x(k|t), u(k|t)), \end{aligned} \tag{17}$$

where $v_\mathrm{l}(k \cdot dt + t + 1)$ is the future speeds of the leader at time $(k \cdot dt + t + 1)$, which is used to generate constraints in the OCP. The above four constraints are:

- upper and lower limits of the follower vehicle position ($\overline{p}$, $\underline{p}$) for keeping a positive inter-vehicular distance and avoiding cut-ins from other lanes, constructed using the leader vehicle's position p_l and speed v_l:

$$\overline{p} = p_\mathrm{l} - 0.3 v_\mathrm{l} \tag{18}$$

$$\underline{p}(s) = \begin{cases} p_\mathrm{l} - (4v_\mathrm{l} + 3), & \text{if } v_\mathrm{l} > 9 \\ p_\mathrm{l} - (10v_\mathrm{l} + 3), & \text{if } 0.7 < v_\mathrm{l} \leq 9 \\ p_\mathrm{l} - 10, & \text{if } v_\mathrm{l} \leq 0.7 \end{cases} . \tag{19}$$

  and this formulation is the same as in [9], except that the distance gap is enlarged by changing the values for the multipliers in (19) and (18), as well as adding the constant offset in (19). These numbers are design parameters and can be adjusted by the user based on the traffic condition and controller performance. Enlarging the distance gap will provide more flexibility in varying the speed and thus will deliver better performance, but traffic capacity will drop [27]. Note that the Heaviside step function can be utilized to formulate the expression for (19). The parameters in (19) and (18) are design parameters and can be changed by the user.
- upper and lower limits of the follower CAV speed, with the upper limit $\overline{v_\mathrm{f}}$ set to be the road speed limit, and the lower limit $\underline{v_\mathrm{f}}$ set to be 0 to enforce a non-negative speed.
- upper and lower limits of the follower CAV acceleration, with $\underline{a_\mathrm{veh}} = -6\mathrm{m/s}^2$ and $\overline{a_\mathrm{veh}} = 6\mathrm{m/s}^2$. The limits are chosen to be twice that of the maximum vehicle acceleration/deceleration driving the FTP drive cycle.

Table 1. Cost functions defined for both EC-MPC optimization scenarios

i	Case name	Objective to minimize	Cost function
1	EC-MPC$_\mathrm{f}$	Fuel	$J_1(k\|t) = \dot{m}_{\mathrm{Fuel}}(k\|t)dt$
2	EC-MPC$_\mathrm{a}$	Acceleration	$J_2(k\|t) = a_{\mathrm{veh}}(k\|t)^2$

- system dynamics, which is explained in detail in Sections 4 and 5.

Through selection of different cost functions, the vehicle speed trajectory can be calculated to optimize a required criterion. For instance, one can select to minimize a_{veh} as done in [7,9] if an energy conscious optimization is of interest. The selection of the cost function impacts the outcome of velocity trajectory and its critical performance parameters, namely, tailpipe NOx and fuel economy. In the following sections, these performance parameters are simulated with the vehicle model presented in Section 2.

4. Conventional Energy Conscious Model Predictive Controller (EC-MPC)

4.1. EC-MPC control strategy

With fuel consumption as the optimization objective, the OCP in (16) can be solved with different energy conscious cost functions to calculate the optimal speed trajectory of the CAV. For instance, the vehicle acceleration is used in [7,9] as a variable correlated with fuel consumption, and in [3,12,28] the fuel consumption model is used for optimal speed planning. In this paper, two cases are studied as benchmarks, where in each of them a cost function from Table 1 is used for optimal fuel speed planning calculated using the predictive controller in (16). Therefore, the cost at every step t

$$\mathbf{J}_i(t) = \sum_{k=0}^{N_\mathrm{P}-1} J_i(k|t), \quad i = \{1,2\}, \tag{20}$$

is used in (16) over a horizon of N_P steps. The problem in (16)-(20) is solved numerically using the optimization command fmincon in Matlab with the sequential quadratic programming algorithm. The sampling time dt is set to 0.1s and then the length of prediction horizon is $(0.1N_\mathrm{P})$ s.

4.2. EC-MPC performance evaluated over FTP drive cycle

Vehicle fuel consumption and NOx emissions simulated using the vehicle model in (2)-(15) with the optimal acceleration from the two EC-MPC controllers are shown in Figure 6 for different prediction horizons. For the lead vehicle, the federal test procedure for light duty vehicles is selected as the desired speed trajectory. Also, the plotted accumulative mass of fuel and tailpipe NOx are normalized with the corresponding values when the vehicle is driven with the nominal FTP speed trajectory. In other words, we are comparing the scenario when the follower vehicle is driving the optimized trajectory with the nominal case when the follower vehicle is driving the leader's drive cycle exactly without any speed planning. The plots in Figure 6(a) indicate that both EC-MPC$_\mathrm{f}$ and EC-MPC$_\mathrm{a}$ can effectively reduce fuel consumption, but at the same time, both of the controllers increase tailpipe NOx emissions compared with the nominal trajectory despite that engine emitted NOx is reduced in most cases due to the drop in SCR efficiency (Figure 6(b)). It is also shown that although EC-MPC$_\mathrm{f}$ performs better in reducing fuel consumption, it generates more engine and tailpipe NOx emissions

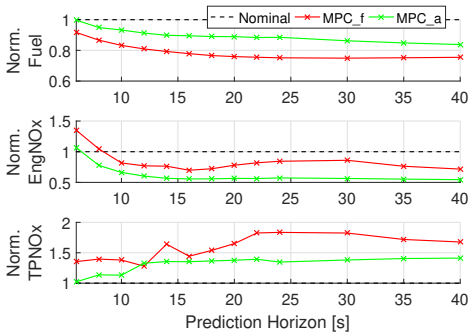

(a) Normalized comparison of the optimal solutions of EC-MPC controllers with different prediction horizons. Fuel consumption, engine out and tailpipe emissions performances are shown in subplots from top to bottom, respectively.

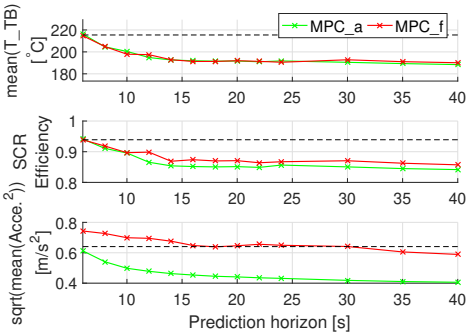

(b) Correlation between cycle-averaged turbine temperature $\overline{T_{\mathrm{TB}}}$, SCR efficiency and vehicle acceleration $\overline{|a|}$, of the optimal trajectories. Lower acceleration level yields lower turbine temperature and lower SCR efficiency.

Figure 6. Results for the follower vehicle with EC-MPC controllers.

compared with EC-MPC$_{\mathrm{a}}$.

With longer prediction horizon in EC-MPC controllers, acceleration level is reduced and, at the same time, cycle-averaged turbine temperature and SCR efficiency are also reduced as shown in Figure 6(b). Due to the lower SCR efficiency, the resulting tailpipe NOx (in Figure 6(a)) does not drop even though the trip acceleration level is reduced.

5. Energy and Emissions Conscious Model Predictive Controller (E^{2}C-MPC)

The conventional CAV speed controllers described in the previous section indicate degraded tailpipe emissions performance despite better fuel economy when the formulation is only energy conscious and emissions are ignored. To avoid this problem, an intuitive solution would be to add an additional constraint to the OCP to limit the follower vehicle's total tailpipe NOx emissions:

$$\sum_{k=0}^{N_{\mathrm{total}}} \{\dot{m}_{\mathrm{NOx.TP}}(k)\}_{\mathrm{MPC}} \cdot dt \leq \sum_{k=0}^{N_{\mathrm{total}}} \{\dot{m}_{\mathrm{NOx.TP}}(k)\}_{\mathrm{Nom}} \cdot dt, \tag{21}$$

where the subscript "MPC" refers to the driving scenario in which the follower CAV drives the optimized trajectory, and "Nom" refers to the nominal driving scenario in which the CAV drives the leader vehicle's drive cycle exactly. This way, the emissions performance could be included in the control loop. Dynamic programming method could be used to solve the OCP with the additional constraint (21) by considering the accumulative NOx as an additional state. However, this solution strategy would be non-causal, since it requires knowledge of the whole drive cycle before starting to solve for the optimal solution. Furthermore, it would be very computationally costly. Thus, optimization problems with this terminal constraint are hard to solve using causal control strategies due to the fact that the summation is calculated over the whole trip. Hence, an alternative strategy is developed in this section that is practically implementable.

5.1. E^2C-MPC design

The emissions constraint in (21) is relaxed to be a soft constraint and embedded into the cost function by adding an additional term to the previous EC-MPC cost function defined in (20), which is the instantaneous emissions scaled by an equivalence factor. This forms the energy and emissions conscious cost:

$$\mathbf{J}_{\mathrm{E^2C\_NOx}}(t) = \sum_{k=0}^{N_\mathrm{P}-1} \left(\dot{m}_\mathrm{fuel}(k|t) + w \cdot \dot{m}_\mathrm{NOx.TP}(k|t)\right) dt. \tag{22}$$

With the cost function defined in (22), the OCP aims to reduce the predicted tailpipe NOx emissions in the prediction horizon in addition to reducing the predicted fuel consumption.

Note that the equivalence factor w should be pre-tuned offline. A method is proposed in [29] to calculate the equivalence factor online by calculating an approximation of the optimal cost-to-go function. This method, however, needs finding the Dynamic Programming solution with high computational burden and with a knowledge of the whole drive cycle. Therefore, an alternative approach is adopted in this paper; namely, we focus on designing the energy and emissions conscious MPC, and identify a range for w that works for most of the well known drive cycles.

The OCP satisfies the same constraint as in (17) with the system dynamics $f(x,u)$ for the state vector $x = \left[p_\mathrm{veh}, v_\mathrm{veh}, T_\mathrm{b.rSCR}\right]^T$, and $T_\mathrm{b.rSCR}$ is the state for SCR brick temperature simulated with a reduced-order model, where the aftertreatment system including SCR is assumed to be lumped into one thermal mass with the following dynamics:

$$T_\mathrm{g.rSCR} = \frac{\frac{\dot{m}_\mathrm{exh} C_\mathrm{pg}}{V_\mathrm{rSCR}} T_\mathrm{TB.ss} + (h_1\alpha_1)_\mathrm{rSCR} T_\mathrm{b.rSCR}}{(h_1\alpha_1)_\mathrm{rSCR} + \frac{\dot{m}_\mathrm{exh} C_\mathrm{pg}}{V_\mathrm{rSCR}}} \tag{23}$$

$$(1-\varepsilon_\mathrm{rSCR})\rho_\mathrm{b} C_\mathrm{b} \frac{dT_\mathrm{b.rSCR}}{dt} = (h_1\alpha_1)_\mathrm{rSCR}(T_\mathrm{g.rSCR} - T_\mathrm{b.rSCR}) - (h_2\alpha_2)_\mathrm{rSCR}(T_\mathrm{b.rSCR} - T_\mathrm{a}) \tag{24}$$

where $T_\mathrm{g.rSCR}$ and $T_\mathrm{b.rSCR}$ in the reduced SCR model are used to approximate outlet gas and brick temperatures $T_\mathrm{g.SCR}$ and $T_\mathrm{b.SCR}$ in the full thermal model. The vehicle longitudinal dynamics and the powertrain model from (1)-(7) remain the same. Note that this reduced SCR model is only used in the MPC and the plant is still simulated with the full thermal model; i.e., the full thermal model is used for evaluating the optimal trajectory and update the initial conditions at each MPC run.

Two considerations are worth highlighting here: (1) The results in Figure 6(b) show that as acceleration increases, fuel consumption increases, but, at the same time, turbine temperature increases as well, which leads to higher SCR temperature and SCR efficiency, and consequently, lower tailpipe NOx. (2) Since the prediction horizon will be limited, we would expect an MPC with a faster dynamics to perform more consistently than that with slower dynamics. From the above observations, increase in turbine temperature could potentially be used as an indication of reduced tailpipe NOx emissions with $\mathrm{MPC_a}$.

Based on these considerations, a second $\mathrm{E^2C}$-MPC formulation is developed as follows in an effort to seek a simpler OCP. In particular, a new cost function $\mathbf{J}_{\mathrm{E^2C\_TB}}(t)$ is introduced, which is obtained by replacing the $\dot{m}_\mathrm{fuel}$ term in (22) with acceleration, and replacing the $m_\mathrm{NOx.TP}(k+t|t)$ term with turbine temperature as follows.

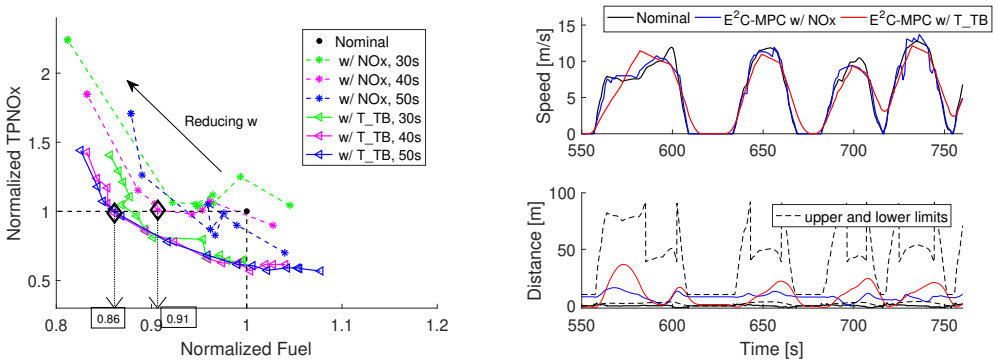

(a) Fuel and emissions reduction effects using E^{2}C-MPC$_{\text{NOx}}$ (labeled with NOx), and E^{2}C-MPC$_{\text{TB}}$ (labeled with T_TB). Different data points on a same curve are due to monotonically varying w.

(b) Optimal trajectories using E^{2}C-MPC$_{\text{NOx}}$ and E^{2}C-MPC$_{\text{TB}}$ with 40s prediction horizon. The two optimized trajectories (correspond to the diamond marked points on the left figure) are chosen such that they have the same tailpipe NOx emissions as the nominal FTP trace.

Figure 7. Comparison of fuel consumption versus TPNOx curves and optimized speed and acceleration trajectories between using E^{2}C-MPC$_{\text{NOx}}$ and E^{2}C-MPC$_{\text{TB}}$.

$$\begin{aligned}\mathbf{J}_{\text{E}^2\text{C\_TB}}(t) &= \sum_{k=0}^{N_{\text{P}}-1}\Big(a(k|t)^2 + w(T_{\text{TB}}(k|t) - T_{\text{thr}})^2 \cdot I_{\text{TB}}(k)\Big), \quad \text{with} \\ I_{\text{TB}}(k) &= \begin{cases} 1, & \text{if } T_{\text{TB}}(k|t) < T_{\text{thr}} \\ 0, & \text{if } T_{\text{TB}}(k|t) \geq T_{\text{thr}} \end{cases},\end{aligned} \tag{25}$$

where T_{thr} is a pre-tuned parameter, which represents the lower desired threshold for the turbine temperature. The OCP satisfies the same constraint as in (17) with the system dynamics $f(x,u)$ for the state vector $x = \left[p_{\text{veh}}, v_{\text{veh}}, T_{\text{TB}}\right]^T$ including (1)-(8). Thus, this formulation, called E^{2}C-MPC$_{\text{TB}}$, aims to reduce acceleration while maintaining turbine temperature. As shown in the next section, this formulation is able to balance fuel consumption and NOx emissions, and it can do so with simpler dynamics that makes solving the OCP numerically easier.

5.2. E^{2}C-MPC performance evaluated over FTP drive cycle

5.2.1. Selection of E^{2}C-MPC optimization criterion

The two E^{2}C-MPC controllers are evaluated over the FTP drive cycle with different length of prediction horizons with results shown in Figure 7. The sampling time dt is increased to 1 s compared with 0.1 s as used in Section 5 to shorten the computation time. For each selected horizon, the equivalence factor w is swept from 0 to 1 to show the trade-off between emissions and fuel consumption. In other words, the multi-objective optimization problem is scalarized to build the Pareto-optimal curve. In each plot, the accumulative fuel and tailpipe NOx values are normalized by their respective nominal values.

End of drive cycle results shown in Figure 7(a) indicate E^{2}C-MPC$_{\text{TB}}$ outperforms E^{2}C-MPC$_{\text{NOx}}$ since (1) the emission-fuel consumption curve is smoother and more monotonic in both fuel and emissions performance, and (2) better fuel economy is obtained at the same level of NOx emissions. One reason for E^{2}C-MPC$_{\text{TB}}$ being more effective than E^{2}C-MPC$_{\text{NOx}}$

Table 2. Reasons for terminating optimization process when solving for optimal trajectories using E^{2}C-MPC$_{\mathrm{NOx}}$ and using E^{2}C-MPC$_{\mathrm{TB}}$ (trajectories are associated with Figure 7(b)), when the optimal control problem is solved with optimization command fmincon in Matlab.

Exit reason	Not feasible	Reaches number of iterations	First-order optimal	Design step size tolerance reached
w/NOx	7%	2%	4%	87%
w/T_{TB}	0%	0%	99%	1%

is that the objective function $\mathbf{J}_{\mathrm{E^2C\_TB}}(t)$ is numerically easier to optimize. The turbine thermal dynamics and the quadratic acceleration terms are less complicated, and have a larger gradient due to faster dynamics than that of the reduced SCR thermal dynamics and the fuel consumption terms. The smooth and predictable NOx and fuel consumption trade-off observed for E^{2}C-MPC$_{\mathrm{TB}}$ offers convenience for calibrating the equivalence factor w for achieving the best fuel economy for a given tailpipe emissions.

Figure 7(b) shows the optimal speed traces and the distance between the two vehicles for the two optimization formulations, E^{2}C-MPC$_{\mathrm{TB}}$ and E^{2}C-MPC$_{\mathrm{NOx}}$, both with a 40 s prediction horizon. The selected points are marked with diamond markers in Figure 7(a), and their equivalence factors are selected such that both MPC controllers generate the same tailpipe NOx emissions as the nominal FTP trace. However, E^{2}C-MPC$_{\mathrm{TB}}$ with 40 s horizon results in 14% better fuel economy, while E^{2}C-MPC$_{\mathrm{NOx}}$ improves the fuel economy by 9% compared to the nominal. This behavior is related to the fact that, as the distance trajectories in Figure 7(b) show, with the E^{2}C-MPC$_{\mathrm{TB}}$ utilized for the optimal speed planning, the advantage of having a flexible following distance is exploited more compared to the E^{2}C-MPC$_{\mathrm{NOx}}$, in which the vehicle distance is almost constant. One reason for this performance difference is that with the more complicated reduced SCR thermal and emissions models involved in the E^{2}C-MPC$_{\mathrm{NOx}}$, it is easier for the optimizer to get stuck at infeasible regions (7%, as shown in Table 2) or not being able to satisfy the first-order optimality conditions before design step size tolerance is reached (87%) compared to E^{2}C-MPC$_{\mathrm{TB}}$ (0% and 1%, respectively). With E^{2}C-MPC$_{\mathrm{TB}}$, the chance of finding the point satisfying the first-order optimality conditions is much higher (99%). Note that if the design step size tolerance is reached before the first-order optimality conditions are met, that means the current point satisfies the constraints and is possibly close to a local optimum, but the violation of the first-order optimality conditions is larger than that required by the optimality tolerance and reducing this violation would require a smaller design step size than the allowed minimum threshold. Also note that the formulation with NOx is using minimum step size as 0.001 m/s^2, while with TB the minimum step size is 0.01 m/s^2, 10 times of that for the NOx formulation. This means that the formulation with NOx has a more sensitive cost function, which explains the more consistent and better performance of E^{2}C-MPC$_{\mathrm{TB}}$ in Figure 7.

The computation time required for calculating the optimal speed over the prediction horizon at each step with E^{2}C-MPC$_{\mathrm{TB}}$ is expected to be reduced significantly due to simplified dynamics when it is compared with E^{2}C-MPC$_{\mathrm{NOx}}$. Table 3 shows the statistical features of computation time for the two OCPs calculated with time step of 1 s. The simulations results are obtained on a desktop computer with an Intel Core i7-7700 CPU at 3.6GHz. The code is written and executed in the Matlab environment with the purpose of comparing the computation time of these two OCPs. It is expected that less computation time can be achieved by re-writing and optimizing the code in a compiled language if run on the same hardware. As shown, with the same prediction horizon, the E^{2}C-MPC$_{\mathrm{TB}}$ with T_{TB} dynamics runs almost 10 times faster than the E^{2}C-MPC$_{\mathrm{NOx}}$ where SCR and NOx models with reduced order thermal dynamics for the aftertreatment system are used.

Table 3. Comparison of statistics calculated from computation time of all optimization steps for E^2C-MPC$_{NOx}$ and for E^2C-MPC$_{TB}$.

MPC Type	w/ NOx				w/ T_{TB}			
Horizon [s]	20	30	40	50	20	30	40	50
Mean [s]	0.62	1.65	3.27	5.39	0.02	0.03	0.05	0.08
Std [s]	0.35	0.75	1.23	1.82	0.01	0.02	0.03	0.07
Max [s]	1.82	4.98	8.18	11.82	0.14	0.28	0.28	0.63

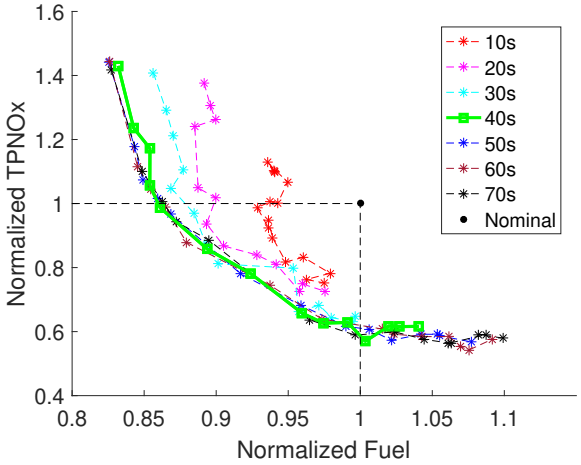

Figure 8. Normalized fuel consumption vs. TPNOx for optimal trajectories with E^2C-MPC$_{TB}$ evaluated over FTP with different selections of w and prediction horizon N_P.

5.2.2. Selection of prediction horizon

The length of the prediction horizon is a design parameter for MPC. Thus, its impact on the E^2C-MPC$_{TB}$ controller is studied and shown in Figure 8 for prediction horizons from 10 s to 70 s. As shown, when the prediction horizon increases from 10 s to 40 s, the normalized Fuel - NOx curve moves towards the left-lower direction, which means less fuel consumption and tailpipe NOx emissions. However, as also shown, increasing the prediction horizon beyond 40 s does not help in saving more fuel or tailpipe NOx, but increases the computational load due to the increased number of optimization variables. Thus, it is concluded that E^2C-MPC$_{TB}$ with a 40 s prediction horizon is an acceptable design to reduce fuel consumption while maintaining emissions performance of the CAV.

5.2.3. Effect of the equivalence factor w

Optimized CAV speed, acceleration trajectories, and histogram of acceleration for two equivalence factors, both with a 40 s prediction horizon, are shown in Figure 9. With larger w, the controller penalizes the acceleration relatively less, and thus results in trajectories with larger accelerations. This is seen more clearly in Figure 9(b), since the acceleration distribution for smaller w is located mostly in the range of $[-1,1]$ m/s^2, while for larger w, this range grows into $[-1.5,1.5]$ m/s^2. On the one hand, the resulting average turbine temperature grows with w as shown in Figure 10(b) as well as the time resolved plot Figure 11(a), as there is higher cost for dropping turbine temperature for larger ws. On the other hand, since the relative penalty on a large acceleration is decreased, a more oscillatory trajectory ensues with larger w and that leads to higher fuel consumption as shown in Figure 10(a). As the result of higher turbine

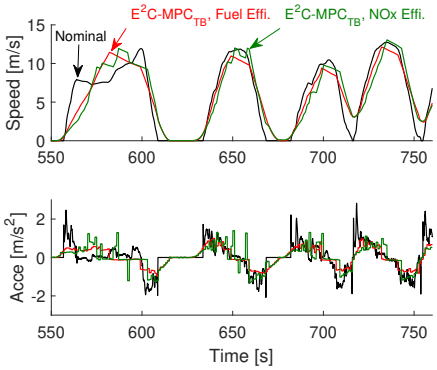

(a) Optimized CAV speed and acceleration traces with two different equivalence factors.

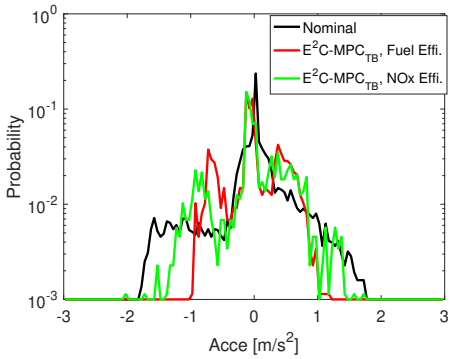

(b) Histograms of optimized CAV acceleration with two different equivalence factors.

Figure 9. Optimization results using E^{2}C-MPC$_{\mathrm{TB}}$ controllers with two different equivalence factors corresponding to a more fuel efficient trajectory ($w = 0.1$) and a more NOx efficient trajectory ($w = 0.6$). The fuel efficient trajectory has the same tailpipe NOx emissions as the nominal trajectory, and the NOx efficient trajectory has the same fuel consumption as the nominal trajectory.

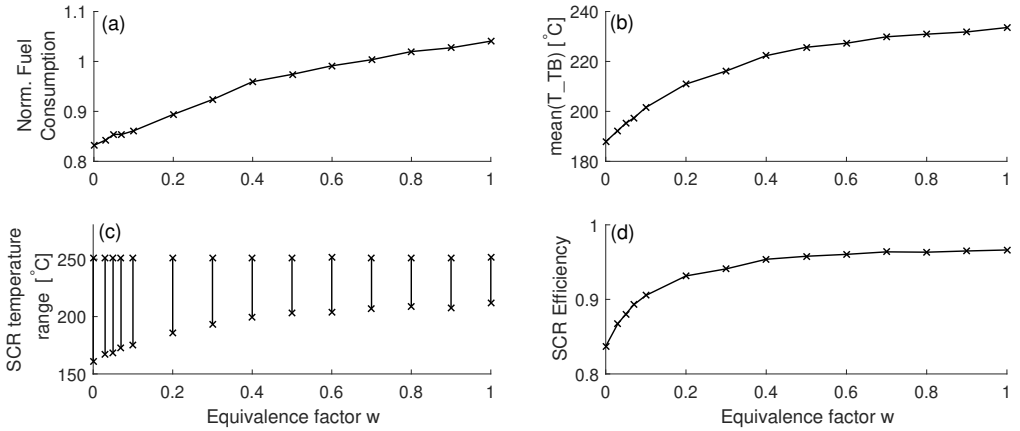

Figure 10. Effect of w on normalized fuel consumption, turbine temperature, SCR temperature range (maximum and minimum SCR temperature) and average SCR efficiency when the controller is applied to the FTP drive cycle.

temperature, SCR temperature is also increased as shown in Figure 11(b), which avoids the large SCR temperature drop to around 160°C as happens with $w = 0$ and could maintain the SCR temperature to stay above 200°C with larger w (Figure 10(c)). This results in a higher average SCR efficiency, as shown in Figure 10(d). Hence, it is inferred that the reason for why increasing w reduces tailpipe NOx emissions as seen in Figure 10(d) is that average SCR efficiency (which is also the average NOx conversion efficiency) increases with the equivalence factor.

5.3. Robustness of E^{2}C-MPC$_{TB}$: performance evaluation over different drive cycles

The robustness of the proposed E^{2}C-MPC controller with the surrogate cost (i.e. E^{2}C-MPC$_{\mathrm{TB}}$) to variations in the drive cycle is evaluated by testing the controller over five additional drive cycles including Heavy Duty FTP (FTPHD), the Supplemental Federal Test Procedure (SC03), Worldwide Harmonised Light Vehicle Test Procedure (WLTP), World Harmonized Vehicle Cycle (WHVC), and New European Driving Cycle (NEDC). Figure 12

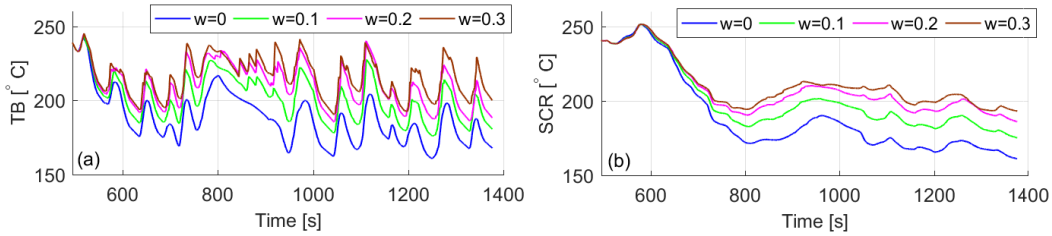

Figure 11. Effect of equivalence factor w on turbine temperature and SCR temperature, shown as time resolved results.

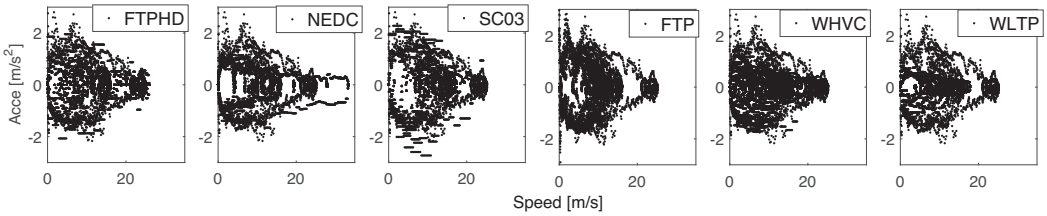

Figure 12. Visitation points of the vehicle speed and acceleration for six different drive cycles commonly used for vehicle certification.

shows the vehicle speed and acceleration visitation points of these six selected drive cycles when the E^{2}C-MPC with 40 s prediction horizon is used to optimize the velocity trajectory. As shown, these six drive cycles span a wide range of vehicle operating conditions.

The temperature of the aftertreatment system at the end of the FTP Bag 1 is selected as the initial condition for all the other cycles for consistent evaluation and comparison to the FTP Bag 2 results presented in the previous sections. Similar to the FTP simulations, it is assumed that a leader vehicle is driving one of the five drive cycles mentioned above, and the follower CAV is using the E^{2}C-MPC$_{\text{TB}}$ controller design to optimize its speed trajectory. The equivalence factor w is swept for each test to generate the normalized Fuel - NOx curves for these trajectories, as shown in Figure 13(a). The fuel consumption and tailpipe NOx values for different tests are normalized by their respective values corresponding to each test's nominal driving scenario.

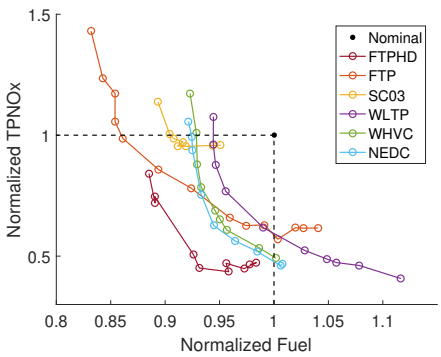

(a) Pareto-shaped fronts observed for normalized fuel consumption versus NOx when testing different drive cycles with E^{2}C-MPC$_{\text{TB}}$ controller design.

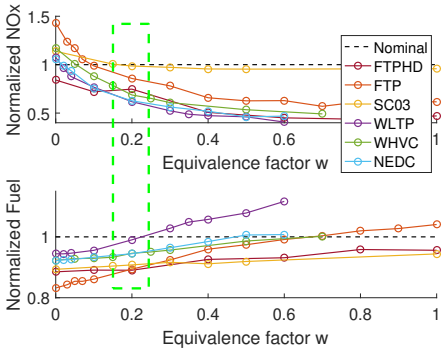

(b) Effect of equivalence factor w on normalized fuel consumption and tailpipe NOx emissions of different drive cycles.

Figure 13. E^{2}C-MPC$_{\text{TB}}$ controller evaluated over different drive cycles.

For all the tested drive cycles, there exist a range of w such that the optimal trajectories have lower fuel consumption and lower tailpipe NOx emissions than the nominal (Figure 13(a)). To visualize this range, the resulting normalized fuel consumption and tailpipe NOx are separately shown at each w in Figure 13(b). As observed, the trend is the same for all trajectories; with increasing equivalence factor, fuel consumption increases and tailpipe NOx emissions decrease. The green dashed box in Figure 13(b) shows the range of the equivalence factor w in the proposed E^2C-MPC$_{TB}$ controller when a selected w is acceptable for all drive cycles; i.e., the E^2C-MPC$_{TB}$ controller with that w will yield an optimal trajectory that is both more fuel efficient and NOx efficient than its leader vehicle's drive cycle. Note that a priori knowledge of the drive cycle would allow for improving the selection of w by performing offline computations to make the optimal trajectory more fuel/emissions efficient. However, if the drive cycle is not known beforehand, choosing the smallest acceptable w will yield a causal controller, which results in 5-15% improvement in the fuel economy with a corresponding 0-25% NOx emissions reduction for these tested cycles. Figure 13(b) also shows that with $w = 0$, the E^2C-MPC$_{TB}$ controller simplifies into the conventional EC-MPC$_a$ and optimized traces for 5 of the 6 tested drive cycles result in more tailpipe NOx emissions than their corresponding leading cycles. This observation confirms that the E^2C-MPC$_{TB}$ controller has better performance in maintaining emissions than the EC-MPC$_a$ controller.

6. Discussion on existing challenges

This paper contributes a model predictive control formulation, namely, E^2C-MPC$_{TB}$, which is able to balance fuel consumption and tailpipe NOx emissions for diesel vehicles that are equipped with SCR-exhaust aftertreatment systems. Ultimately, this controller is aimed at reducing fuel and emissions for on-road connected and automated vehicles. Acquisition of the velocity preview of the leader vehicle is not considered in this paper; however, in practice, speed prediction within the future 40 s is not a trivial task in real driving conditions. The literature offers multiple speed prediction methods with current and past information [30,31], or with additional information from leader vehicles and infrastructure [32]. For example, authors of [32] compare the performances of deterministic MPC, chance constrained MPC and randomized MPC when predicted speed information is utilized to plan for fuel efficient trajectory in a car-following scenario. They introduce slack variables to represent violations of the distance constraint to avoid infeasible solutions, and show that chance constrained MPC performs well in improving fuel efficiency, driving comfort and avoiding collisions. The E^2C-MPC$_{TB}$ with a hard distance constraint can be also dealt with in a similar manner if speed preview is generated by some predictors.

Other two existing gaps for real-road implementation is real-time implementability of the nonlinear MPC and the assumption that the follower vehicle could satisfy all the traffic rules by following the leader vehicle. For the first issue, despite that E^2C-MPC$_{TB}$ is significantly faster than the original E^2C-MPC$_{NOx}$ formulation, its computation speed on a real control hardware has not been tested in this work. One possible way to transform the nonlinear MPC into a problem that can be solved in real-time in a vehicle control unit, e.g., is mentioned in [33], where authors provide a way to solve the nonlinear MPC problem approximately by transforming it online into quadratic programming problems that require computation times that are sometimes only marginally larger than linear MPC.

For the second issue, the controller presented in this work is not capable of dealing with cases where the follower vehicle needs to stop at either stop signs or traffic intersections, when the leader vehicle passes. Other works have presented control strategies to use vehicle-to-vehicle communication and signal phasing and timing information to develop fuel efficient

speed trajectories for automated vehicles through travelling at fuel efficient speeds and avoiding red lights by tracking a target velocity designed based on timing and position information of the upcoming traffic light [10]. Potentially, a similar idea can also be applied here by removing the distance constraint and adding a velocity tracking term in the cost function, when there is no leader vehicle or the vehicle is near to a traffic light. The applicability of such techniques in the context of this work is an open research question.

7. Conclusion

An energy and emissions conscious model predictive control formulation is developed to increase fuel economy without compromising emissions in a diesel CAV by planning an optimal speed trajectory based on a given leader drive cycle and a flexible following distance between the two vehicles. Simulation results with a validated medium duty diesel truck model confirm that the new formulation can achieve 5-15% improvement in the fuel economy with a corresponding 0-25% NOx emissions reduction in all the drive cycles tested. This performance is shown to be in contrast to the conventional energy conscious formulation that focuses on only fuel economy and thus its good performance in fuel economy improvement is always accompanied by a penalty in emissions performance. The new formulation's design parameters, namely, the prediction horizon and the equivalence factor, are studied to understand their impact on the controller's performance, and it is found that a good performance can be achieved with the same design parameters across all the drive cycles tested, where a good performance means improved fuel economy without a reduction, and in fact often an improvement, in NOx emissions performance. The analysis of the computational performance of the new controller reveals that an online implementation could be feasible. Hence, the results encourage further development and experimental testing of this controller. Important challenges for the proposed method are that accurate information of the lead vehicle speed within the future 40 s is required to use the predictive controller for speed planning, and to honor traffic rules which are not captured by following the leader vehicle. Analyzing the effect of inaccurate prediction on E^2C-MPC performance and developing remedies to minimize the expected deterioration in performance and to honor additional traffic rules are identified as important future research directions.

Acknowledgment

The authors would like to thank Michiel Van Nieuwstadt and Cory Hendrickson from Ford Research and Advanced Engineering for providing valuable data and technical suggestions.

Disclosure statement

No potential conflict of interest was reported by the authors.

Funding

This material is based upon work supported by the National Science Foundation under Grant No. 1646019.

References

[1] Tate L, Hochgreb S, Hall J, et al. Energy efficiency of autonomous car powertrain. SAE Technical Papers; 2018. 2018-01-1092.

[2] Asadi B, Vahidi A. Predictive cruise control: Utilizing upcoming traffic signal information for improving fuel economy and reducing trip time. IEEE transactions on control systems technology. 2011;19(3):707–714.

[3] Schmied R, Waschl H, Quirynen R, et al. Nonlinear MPC for emission efficient cooperative adaptive cruise control. IFAC-Papersonline. 2015;48(23):160–165.

[4] Moser D, Schmied R, Waschl H, et al. Flexible spacing adaptive cruise control using stochastic model predictive control. IEEE Transactions on Control Systems Technology. 2018;26(1):114–127.

[5] Huang C, Salehi R, Stefanopoulou AG. Intelligent cruise control of diesel powered vehicles addressing the fuel consumption versus emissions trade-off. In: 2018 Annual American Control Conference (ACC); IEEE; 2018. p. 840–845.

[6] Li S, Li K, Rajamani R, et al. Model predictive multi-objective vehicular adaptive cruise control. IEEE Transactions on Control Systems Technology. 2011;19(3):556–566.

[7] Mahler G, Vahidi A. An optimal velocity-planning scheme for vehicle energy efficiency through probabilistic prediction of traffic-signal timing. IEEE Transactions on Intelligent Transportation Systems. 2014;15(6):2516–2523.

[8] Al Alam A, Gattami A, Johansson KH. An experimental study on the fuel reduction potential of heavy duty vehicle platooning. In: Intelligent Transportation Systems (ITSC), 2010 13th International IEEE Conference on; IEEE; 2010. p. 306–311.

[9] Prakash N, Cimini G, Stefanopoulou AG, et al. Assessing fuel economy from automated driving: Influence of preview and velocity constraints. In: ASME 2016 Dynamic Systems and Control Conference; American Society of Mechanical Engineers; 2016. p. V002T19A001–V002T19A001.

[10] HomChaudhuri B, Vahidi A, Pisu P. Fast model predictive control-based fuel efficient control strategy for a group of connected vehicles in urban road conditions. IEEE Transactions on Control Systems Technology. 2017 March;25(2):760–767.

[11] Alam A, Martensson J, Johansson KH. Look-ahead cruise control for heavy duty vehicle platooning. In: Intelligent Transportation Systems-(ITSC), 2013 16th International IEEE Conference on; IEEE; 2013. p. 928–935.

[12] Stanger T, del Re L. A model predictive cooperative adaptive cruise control approach. In: American Control Conference (ACC), 2013; IEEE; 2013. p. 1374–1379.

[13] Huang C, Salehi R, Ersal T, et al. Optimal speed planning using limited preview for connected vehicles with diesel engines. In: 14th International Symposium on Advanced Vehicle Control; 2018.

[14] United States Environmental Protection Agency. Protection of environment, 40 C.F.R ; 2018.

[15] Guo J, Ge Y, Hao L, et al. Comparison of real-world fuel economy and emissions from parallel hybrid and conventional diesel buses fitted with selective catalytic reduction systems. Applied energy. 2015;159:433–441.

[16] Polterauer P, Del Re L. Emission constrained fuel optimal vehicle control with route lookahead. In: 2018 Annual American Control Conference (ACC); IEEE; 2018. p. 5510–5515.

[17] Wang Z, Chen X, Ouyang Y, et al. Emission mitigation via longitudinal control of intelligent vehicles in a congested platoon. Computer-Aided Civil and Infrastructure Engineering. 2015; 30(6):490–506.

[18] Kum D, Peng H, Bucknor NK. Optimal energy and catalyst temperature management of plug-in hybrid electric vehicles for minimum fuel consumption and tail-pipe emissions. IEEE Transactions on Control Systems Technology. 2013;21(1):14–26.

[19] Tschopp F, Nüesch T, Wang M, et al. Optimal energy and emission management of a diesel hybrid electric vehicle equipped with a selective catalytic reduction system. SAE, Warrendale, PA; 2015. 2015-24-2548.

[20] Nüesch T, Cerofolini A, Mancini G, et al. Equivalent consumption minimization strategy for

the control of real driving NOx emissions of a diesel hybrid electric vehicle. Energies. 2014; 7(5):3148–3178.
[21] Cavataio G, Jen HW, Warner JR, et al. Enhanced durability of a Cu/zeolite based SCR catalyst. SAE International Journal of Fuels and Lubricants. 2008;1(2008-01-1025):477–487.
[22] Chen P, Wang J. Control-oriented model for integrated diesel engine and aftertreatment systems thermal management. Control Engineering Practice. 2014;22:81–93.
[23] Lepreux O, Creff Y, Petit N. Motion planning for a diesel oxidation catalyst outlet temperature. In: 2008 American Control Conference; IEEE; 2008. p. 2092–2098.
[24] Bresch-Pietri D, Leroy T, Petit N. Control-oriented time-varying input-delayed temperature model for si engine exhaust catalyst. In: American Control Conference (ACC), 2013; IEEE; 2013. p. 2189–2195.
[25] Pandey V, Jeanneret B, Gillet S, et al. A simplified thermal model for the three way catalytic converter. In: TAP 2016, 21st International Transport and Air Pollution Conference; 2016. p. 6 p.
[26] Cavataio G, Jen HW, Warner JR, et al. Enhanced durability of a cu/zeolite based scr catalyst. SAE International Journal of Fuels and Lubricants. 2009;1(1):477–487.
[27] Lang D, Stanger T, Schmied R, et al. Predictive cooperative adaptive cruise control: Fuel consumption benefits and implementability. In: Optimization and optimal control in automotive systems. Springer; 2014. p. 163–178.
[28] He CR, Maurer H, Orosz G. Fuel consumption optimization of heavy-duty vehicles with grade, wind, and traffic information. Journal of Computational and Nonlinear Dynamics. 2016; 11(6):061011.
[29] Zentner S, Asprion J, Onder C, et al. An equivalent emission minimization strategy for causal optimal control of diesel engines. Energies. 2014;7(3):1230–1250.
[30] Lefèvre S, Sun C, Bajcsy R, et al. Comparison of parametric and non-parametric approaches for vehicle speed prediction. In: 2014 American Control Conference; IEEE; 2014. p. 3494–3499.
[31] Sun C, Hu X, Moura SJ, et al. Velocity predictors for predictive energy management in hybrid electric vehicles. IEEE Transactions on Control Systems Technology. 2014;23(3):1197–1204.
[32] Moser D, Schmied R, Waschl H, et al. Flexible spacing adaptive cruise control using stochastic model predictive control. IEEE Transactions on Control Systems Technology. 2017;26(1):114–127.
[33] Gros S, Zanon M, Quirynen R, et al. From linear to nonlinear mpc: bridging the gap via the real-time iteration. International Journal of Control. 2016;:1–19.